The Journal of Physiology

Aquaporin-4 deletion leads to reduced infarct volume and increased peri-infarct astrocyte reactivity in a mouse model of cortical stroke

Nadia Skauli[1], Negar Zohoorian[1], Shervin Banitalebi[1], Samuel Geiseler[2], Maher Salameh[1], Shreyas B. Rao[1], Cecilie Morland[3], Ole P. Ottersen[1] and Mahmood Amiry-Moghaddam[1]

[1]*Division of Anatomy, Department of Molecular Medicine, Institute of Basic Medical Sciences, University of Oslo, Blindern, Oslo, Norway*
[2]*Cardiovascular Research Group IMB, Department of Medical Biology, Faculty of Health Sciences, UiT – The Arctic University of Norway, Tromsø, Norway*
[3]*Section for Pharmacology and Pharmaceutical Biosciences, Department of Pharmacy, The Faculty of Mathematics and Natural Sciences, University of Oslo, Oslo, Norway*

Handling Editors: Laura Bennet & Justin Dean

The peer review history is available in the Supporting Information section of this article (https://doi.org/10.1113/JP284099#support-information-section).

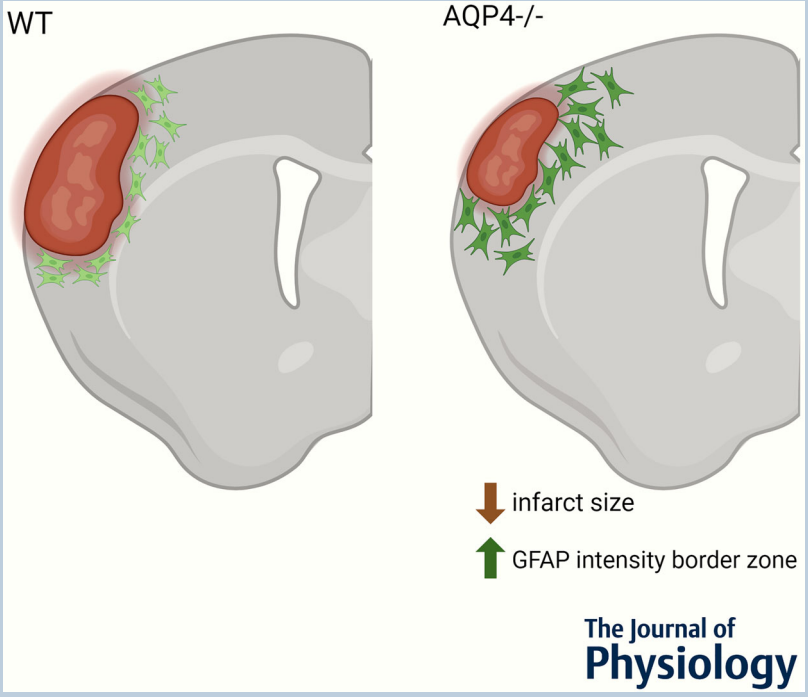

Abstract Aquaporin-4 (AQP4) is the main water channel in brain and is enriched in perivascular astrocyte processes abutting brain microvessels. There is a rich literature on the role of AQP4 in experimental stroke. While its role in oedema formation following middle cerebral artery occlusion (MCAO) has been studied extensively, its specific impact on infarct volume remains unclear. This study investigated the effects of total and partial AQP4 deletion on infarct volume in mice subjected to distal medial cerebral artery (dMCAO) occlusion. Compared to MCAO, this model induces

This article forms part of the 'Aquaporins in Health and Disease' symposium held at Copenhagen in September 2022, and organised by Robert Fenton.

N. Skauli and N. Zohoorian, Joint first authorship.

 DOI: 10.1113/JP284099

smaller infarcts confined to neocortex, and less oedema. We show that AQP4 deletion significantly reduced infarct volume as assessed 1 week after dMCAO, suggesting that the role of AQP4 in stroke goes beyond its effect on oedema formation and dissolution. The reduction in infarct volume was associated with increased astrocyte reactivity in the peri-infarct areas. No significant differences were observed in the number of microglia among the genotypes. These findings provide new insights in the role of AQP4 in ischaemic injury indicating that AQP4 affects both infarct volume and astrocyte reactivity in the peri-infarct zone.

(Received 31 December 2023; accepted after revision 29 May 2024; first published online 24 June 2024)
Corresponding author M. Amiry-Moghaddam: Division of Anatomy, Department of Molecular Medicine, Institute of Basic Medical Sciences, University of Oslo, Post box 1105, Blindern, 0317 Oslo, Norway. Email: mahmo@medisin.uio.no

Abstract figure legend Infarct size and astrocyte reactivity in wild-type (WT) mice compared with AQP4 knockout ($AQP4^{-/-}$) littermates, following distal medial cerebral artery occlusion. Genetic deletion of *Aqp4* ($AQP4^{-/-}$) results in reduced infarct size and heightened astrocyte reactivity, as evidenced by increased glial fibrillary acidic protein (GFAP) immunostaining in the infarct border zone.

Key points

- Aquaporin-4 (AQP4) is the main water channel in brain and is enriched in perivascular astrocyte processes abutting microvessels.
- A rich literature exists on the role of AQP4 in oedema formation following middle cerebral artery occlusion (MCAO).
- We investigated the effects of total and partial AQP4 deletion on infarct volume in mice subjected to distal medial cerebral artery occlusion (dMCAO), a model inducing smaller infarcts confined to neocortex and less oedema compared to MCAO.
- AQP4 deletion significantly reduced infarct volume 1 week after dMCAO, suggesting a broader role for AQP4 in stroke beyond oedema formation.
- The reduction in infarct volume was associated with increased astrocyte reactivity in the peri-infarct areas, while no significant differences were observed in the number of microglia among the genotypes.
- These findings provide new insights into the role of AQP4 in stroke, indicating that AQP4 affects both infarct volume and astrocyte reactivity in the peri-infarct zone.

Introduction

Stroke is a leading cause of mortality and long-term disability worldwide, and continues to pose a significant challenge in clinical medicine (Moskowitz et al., 2010). The pathophysiology of ischaemic stroke involves a complex interplay of various cellular and molecular processes, including excitotoxicity, oxidative stress,

Nadia Skauli is molecular biologist and medical student. She received her Master's degree in Molecular Biosciences in 2015, focusing on monogenic disorders in paediatric neurodegenerative diseases. **Negar Zohoorian** received her Master's degree in Molecular Biosciences in 2019 working on characterizing putative disease-causing mutations in rare syndromes with neurological symptoms. She currently works as a scientist specializing in radiopharmaceuticals. **Shervin Banitalebi** is a medical student in his final year who through the medical student research programme is working on innate inflammatory response after stroke and traumatic injury. All are currently working towards their doctorates in the Laboratory for Molecular Neuroscience at the Medical Faculty of the University of Oslo. The authors explore the mechanisms governing aquaporin-4 expression and polarization, with an emphasis on the roles of this water channel in neuroinflammation. The findings may lead to insights valuable for the development of new treatments for neurodegenerative diseases.

inflammation and oedema formation (Buckley et al., 2013; Chamorro et al., 2016; Iadecola & Anrather, 2011).

Aquaporin-4 (AQP4), a member of the aquaporin family, is strongly expressed in astrocytes within the central nervous system (CNS) (Frigeri et al., 1995; Nielsen et al., 1997). AQP4 is believed to play a crucial role in physiological processes such as regulating water homeostasis, maintaining the volume of the brain's extracellular space, and facilitating the glymphatic system (Amiry-Moghaddam & Ottersen, 2003; Haj-Yasein et al., 2012; Iliff et al., 2012; Nagelhus & Ottersen, 2013; Papadopoulos & Verkman, 2013). Immunogold analyses at the electron microscopic level showed that the distribution of AQP4 is especially dense at the perivascular astrocytic membrane domains that face microvessels (Amiry-Moghaddam et al., 2004; Nielsen et al., 1997).

Previous studies using experimental stroke models have shown that mice with a total AQP4 knockout (Manley et al., 2000) or selective loss of the perivascular pool of AQP4 (Amiry-Moghaddam et al., 2003) exhibit significantly reduced oedema formation. The decrease in oedema formation has been attributed to the role of AQP4 as a membrane channel that mediates bidirectional flow of water (Papadopoulos & Verkman, 2007). Importantly, loss of perivascular AQP4 not only restricts oedema formation after stroke but also reduces infarct size (Amiry-Moghaddam et al., 2003). A similar effect on infarct size has also been observed after total AQP4 knockout (Hirt et al., 2017; Yao et al., 2015). All of these studies relied upon the use of the medial cerebral artery occlusion (MCAO) model, which produces rather extensive infarcts and severe oedema affecting both cortex and the underlying striatum. Thus there is a need to address the protective effect of AQP4 deletion in more sophisticated stroke models with fewer compounding factors. If such models reproduce the protective effect of AQP4 loss, it will be of interest to explore the mechanisms responsible for the reduced infarct size.

In this study, we investigated for the first time the impact of partial and complete AQP4 knockout on infarct size after distal middle cerebral artery occlusion (dMCAO), which induces cortical infarctions of smaller size and with less oedema compared to the MCAO model (Doyle & Buckwalter, 2014). Our findings demonstrate that AQP4 knockout significantly reduces the size of the infarct in this model. Furthermore, in AQP4$^{-/-}$ mice we observed a higher intensity of glial fibrillary acidic protein (GFAP), indicative of increased astrocyte reactivity, in the peri-infarct zone. In contrast, AQP4 deletion did not lead to any changes in microglial activation after stroke. These results indicate that AQP4 has a role in the pathophysiology of stroke that extends beyond its involvement in oedema formation and that may be coupled to astrocyte activation.

Methods

Animals and ethical approval

Male and female adult 3- to 6-month-old C57/BL6J mice (The Jackson Laboratory, Bar Harbor, ME, USA) and mice with homozygous or heterozygous deletion of *Aqp4* bred on a C57/BL6J background were used in this study. AQP4$^{-/-}$ mice were generated as previously described (Thrane et al., 2011). AQP4$^{-/-}$ mice were crossed with wild-type (WT) mice to generate mice heterozygous for AQP4$^{+/-}$. The mice had *ad libitum* access to food and water. All animal experiments were performed according to the European Council Law on Protection of Laboratory Animals, and were approved by The Norwegian Animal Research Authority (NARA), project licence numbers FOTS 8572 and 23017.

Distal middle cerebral artery occlusion

Permanent distal middle cerebral artery occlusions (dMCAO) were performed on the mice (WT; $n = 10$, AQP4$^{-/+}$; $n = 10$, AQP4$^{-/-}$; $n = 10$) as previously described (Banitalebi et al., 2022; Geiseler et al., 2024). In brief, after anaesthetizing animals with isoflurane gas, the skin was cut and cranium was opened to expose the distal middle cerebral artery located downstream of the lenticulostriate arteries. Electrocoagulation of the middle cerebral artery (MCA) bifurcation was performed at three regions. A post-operative analgesia containing buprenorphine 0.1 mg/kg was intraperitoneal injected after 24 h and then daily for 4 days. Water and food were provided *ad libitum*. One week post-surgery, the animals at 2 months age were deeply anaesthetized with intraperitoneal ZRF (zolazepam 3.3 mg/ml, tiletamine 3.3 mg/ml, xylazine 0.5 mg/ml, fentanyl 2.6 μg/ml) (1 ml/g), euthanized by intracardial perfusion fixation using 2% ice-cold dextran followed by 15 min 4% formaldehyde.

Real-time quantitative PCR

Brains from WT ($n = 5$), AQP4$^{+/-}$ ($n = 5$) and AQP4$^{-/-}$ ($n = 5$) mice were regionally dissected and total RNA extracted from parietal cortex and hippocampus by using the RNeasy Plus Mini Kit (Qiagen, Hilden, Germany). RNA concentrations were quantified by NanoDrop (Thermo Fisher Science, Waltham, MA, USA). Reverse transcription of total RNA to cDNA was carried out with Oligo (dT)15 using the GoScript Reverse Transcription System (Promega, Madison, WI, USA). The cDNA was diluted to 2.5 ng/μL in 10 mM Tris–HCl (pH 8.0). Real time PCR was performed using 5 ng cDNA input as previously described (Rao et al., 2019). Reverse transcriptase negative (RTN) and non-template controls (NTC) were

Table 1. Primers for RT-qPCR

Target	Forward primer (5′–3′)	Reverse primer (5′–3′)
Aqp4	*TTTGGACCCGCAGTTATCAT*	*GTTGTCCTCCACCTCCATGT*
H2afz	*ACAGCGCAGCCATCCTGGAGTA*	*TTCCCGATCAGCGATTTGTGGA*
Ppia	*CGCGTCTCCTTCGAGCTGTTTG*	*TGTAAAGTCACCACCCTGGCACAT*
Actb	*GCTCTTTTCCAGCCTTCCTT*	*GTGCTAGGAGCCAGAGCAGT*

included on each plate. Primers used are listed in Table 1. Each transcript was compared to a standard and absolute quantification performed. Housekeeping genes, *H2afz*, *Ppia* and *Actb*, were evaluated by NormFinder and normalization was performed with a combination of *Ppia* and *Actb*, with the best stability value of 0.069.

Preparation of total protein lysates

Animals were deeply anaesthetized with isoflurane and decapitated. The brain was dissected out and parietal cortex and hippocampus were dissected out from AQP4$^{-/-}$, AQP4$^{+/-}$, and WT mice and flash frozen in liquid nitrogen ($n = 5$ for each genotype). The tissues were homogenized in RIPA buffer with freshly added 1× SigmaFAST protease inhibitor (Sigma-Aldrich, St Louis, MO, USA) and 1× PhosSTOP phosphatase inhibitor (Roche Life Science, Basel, Switzerland). Homogenates were incubated on ice for 60 min before centrifugation at 22,000 *g* at 4°C for 15 min. The supernatant was collected as the total protein fraction and concentrations measured using a Pierce BCA protein assay kit (Thermo Fisher Scientific, Waltham, MA, USA).

SDS-PAGE and western blot

SDS-PAGE and western blot was performed as previously described (Katoozi et al., 2017) with some modifications. For analysis of AQP4, 20 μg protein from parietal cortex and hippocampus was prepared and heated in 1× Laemmli loading dye at 37°C for 10 min. For analysis of IBA1 and GFAP, 40 μg protein was used. SDS-PAGE was performed with 4%–20% Tris-Glycine TGX gels (Bio-Rad Laboratories, Hercules, CA, USA) at 160 V for 1 h. The gels were blotted to polyvinylidene difluoride membranes at 100 V for 45 min. Even protein transfer was confirmed with reversible Ponceau S staining before blocking in 5% bovine serum albumin in 1× Tris-buffered saline for 60 min. Membranes were incubated with primary rabbit anti-AQP4 antibody, goat anti-IBA1 antibody, and mouse anti-GFAP antibody from mouse overnight at 4°C. Secondary antibody incubations was performed for 1 h with donkey anti-rabbit horse radish peroxidase (HRP) before Tris-buffered saline with 0.1% Tween-20 (TBST) washes and development with SuperSignal West Pico Chemiluminescent Substrate (Thermo Fisher Scientific). A list of primary and secondary antibodies used for the western blotting experiments is provided in Table 2. Bands were detected on a ChemiDoc Touch Imaging System (Bio-Rad). Membranes were incubated with either rabbit anti-α-tubulin for 1 h or mouse anti-glyceraldehyde 3-phosphate dehydrogenase (GAPDH) overnight for development of control bands. Bands were quantified as arbitrary background-subtracted density units in Image Studio Lite (Ver 5.2, Li-COR Biosciences, Lincoln, NE, USA). Analysis was performed on non-overexposed images; strongly exposed images are presented in the figure only for clarity. Intensities were normalized by dividing the intensities of protein of interest bands with the normalizing control band.

Perfusion and tissue preparation for electron microscopy

A total of seven mice (WT; $n = 3$ and AQP4$^{+/-}$; $n = 4$) were used in these experiments. Mice were deeply anaesthetized with an intraperitoneal injection of Zoletil mixture and transcardially perfused with a solution of 4% formaldehyde in 0.1 M phosphate buffer (PB) and 0.1% glutaraldehyde in 0.1 M PB as described (Hoddevik et al., 2017). The brains were dissected out, post-fixed overnight in the fixation solution, and later stored in a 1:10 dilution of the same solution.

Tissue embedding for electron microscopy

Tissue blocks of 0.5–1 mm in dimension were cut from parietal cortex and hippocampus. The tissue blocks were cryoprotected in 4% glucose in 0.1 M PB overnight followed by suspending the blocks in a graded glycerol solution (10%, 20% and 30% glycerol in 0.1 M PB, 30 min for each gradient). Following cryoprotection, the tissue blocks were rapidly frozen in liquid propane cooled to −170°C and subjected to freeze substitution. Methacrylate resin (Lowicryl HM20, 23994-225, Polysciences Inc., Warrington, PA, United States) was used to embed the specimens, which were subjected to UV light for polymerization below 0°C as previously described Rao

Table 2. Antibodies used for western blotting

Protein	Origin	Category ID	Vendor	RRID	Concentration
Primary antibodies					
AQP4	Rabbit	A5971	Sigma-Aldrich	AB_258 270	1:5000
IBA1	Goat	ab5076	Abcam	AB_2 224 402	1:1000
GFAP	Mouse	MAB360	Millipore	AB_11 212 597	1:5000
α-Tubulin	Rabbit	ab4074	Abcam	AB_2 288 001	1:5000
GAPDH	Mouse	ab9484	Abcam	AB_307 274	1:5000
Secondary antibodies					
Anti-rabbit HRP	Donkey	NA934	GE Healthcare	AB_772 206	1:25 000
Anti-mouse HRP	Sheep	NA931	GE Healthcare	AB_772 210	1:25 000
Anti-goat HRP	Donkey	PA1-28 664	Thermo Fisher Scientific	AB_10 990 162	1:25 000

Abcam, Cambridge, UK; GE Healthcare, Chicago, IL, USA; Millipore, Burlington, MA, USA; Sigma-Aldrich, St Louis, MO, USA; Thermo Fisher Scientific, Waltham, MA, USA. RRID: Research Resource Identifiers

et al. (2019). Ultrathin sections of 80–100 nm were cut using an ultratome (Reichert Ultracut S, Leica Biosystems, Nußloch, Germany) and the sections were placed on 300 mesh grids.

Immunogold cytochemistry

Immunogold labelling was performed as previously described by Mathiisen et al. (2006). Briefly, the sections were incubated overnight with primary antibody (1:400, Sigma-Aldrich; cat. no. A5971; RRID:AB_258270), followed by incubation with secondary goat anti-rabbit antibody coupled to 15 nm colloidal gold particles (1:20 dilution; Abcam, Cambridge, UK; cat. no. ab27236; RRID:AB_954 457; for the quantitative analysis 1:200 dilution was used) for 90 min. For the quantitative analysis, the secondary antibody was used in a 1:200 dilution. The sections were contrasted with 2% uranyl acetate and 0.3% lead citrate for 90 s each. The sections were dried thoroughly before they were examined under the transmission electron microscope (Tecnai 12, FEI Company, Eindhoven, the Netherlands) at 80 kV.

Immunogold quantification and data analysis

For hippocampus, 30–40 capillaries were randomly selected at a magnification of ×2250 between dentate gyrus and stratum radiatum and images were acquired at ×20,500 magnification. The images were obtained from a predetermined side of each capillary to get both end-feet areas and pericytes. A total of 362 images were taken from the hippocampus, and 348 were quantified based on inclusion and exclusion criteria. In the parietal cortex sections, 30–40 capillaries were randomly selected as described above. Subpial regions at the cortical surface were also examined. Exclusion criteria for both the parietal cortex and hippocampus were larger vessels or capillaries with destroyed basement membranes. Images where it was not possible to draw the membrane line in the quantification program were also excluded. The sections were blinded while acquiring the images and during analysis. Immunogold quantification and data analysis was performed by a MATLAB (MathWorks, Natick, MA, USA; R2018b) particle counter toolbox for analysing of immunogold labelled micrographs (Enger, 2017).

Serial tissue sectioning for light microscopy analysis

Prior to sectioning, to cryo-protect the brains, they were sequentially immersed in 10%, 20% and 30% sucrose solutions. Next, the brains were serially sectioned fronto-occipitally into coronal sections of 30 μm thick using an HM 450 freeze microtome (Microm, Walldorf, Germany) and kept in 0.1 M PB. Serial sections throughout the infarction were mounted on gelatin-coated slides before Cresyl Violet staining or immunostaining.

Determination of the infarct volume

For measurement of the infarct volume, 15–30 serial sections (depending on the infarct size), with an interval of five sections, from WT ($n = 10$), AQP4$^{+/-}$ ($n = 9$) and AQP4$^{-/-}$ ($n = 9$) mice were mounted on gelatin-coated slides and stained with Cresyl Violet. Briefly, slides were washed in tap water to remove any residual salts. Then 150 ml of 0.2 M acetic acid was mixed with 100 ml 0.2 M sodium acetate with pH 4.45; 100 ml of the previous buffer was added to 10 ml of Cresyl Echt Violet (1.0%, Aqueous) (Nordic BioSite, Täby, Sweden), and sections were stained for 20 min and rinsed quickly in distilled water. Next, slides were placed in 95% ethyl alcohol for 2 min then in *n*-butyl alcohol with two changes for 2 min. Slides were immersed in xylene with two changes for 2 min

Table 3. Antibodies used for immunolabeling

Protein	Origin	Category ID	Vendor	RRID	Concentration
Primary antibodies					
AQP4	Rabbit	A5971	Sigma-Aldrich	AB_258 270	1:500
IBA1	Goat	ab5076	Abcam	AB_2 224 402	1:100
GFAP	Chicken	PCK-591P	Nordic BioSite	AB_291 542	1:500
iNOS	Mouse	ab49999	Abcam	AB_881 438	1:100
CD206	Rabbit	ab64693	Abcam	AB_1 523 910	1:200
Arg1	Rabbit	#93668	Cell Signaling Technology	AB_2 800 207	1:200
CD16/32	Rat	#80366	Cell Signaling Technology	AB_3 076 525	1:200
LCN2	Rat	ab70287	Abcam	AB_2 136 473	1:200
Secondary antibodies					
Cy2 anti-rabbit	Donkey	711-225-152	Jackson ImmunoResearch Laboratories	AB_2 340 612	1:250
Cy3 anti-rabbit	Donkey	711-165-152	Jackson ImmunoResearch Laboratories	AB_2 307 443	1:250
AF488 anti-goat	Donkey	A11055	Thermo Fisher Scientific	AB_2 534 102	1:250
Cy3 anti-goat	Donkey	705-165-147	Jackson ImmunoResearch Laboratories	AB_2 307 351	1:250
Cy5 anti-chicken	Donkey	703-175-155	Jackson ImmunoResearch Laboratories	AB_2 340 365	1:250
Cy2 anti-mouse	Donkey	715-225-151	Jackson ImmunoResearch Laboratories	AB_2 340 827	1:250
Cy2 anti-chicken	Donkey	703-225-155	Jackson ImmunoResearch Laboratories	AB_2 340 370	1:250
Cy3 anti-rat	Donkey	712-165-150	Jackson ImmunoResearch Laboratories	AB_2 340 666	1:250

Abcam, Cambridge, UK; Cell Signaling Technology, Danvers, MA, USA; Jackson ImmunoResearch Laboratories, West Grove, PA, USA; Nordic Biosite, Täby, Sweden; Thermo Fisher Scientific, Waltham, MA, USA.

and mounted using Eukitt Quick-hardening mounting medium (Sigma-Aldrich). The stained sections were then scanned using AxioScan Z1 (Carl Zeiss Microscopy, Jena, Germany), and infarcted area (visible by relative paleness of Cresyl Violet stain), area of the non-infarcted ipsilateral isocortex and isocortex contralateral to the lesion of the lesion were measured in ImageJ (version; Java 1.8.0-172) (Schneider et al., 2012). Isocortex boundaries in each section was determined by aligning the scanned section to Allen Mouse Brain Atlas (mouse.brain-map.org and atlas.brain-map.org).

The infarct volume was measured indirectly, making it independent of the extent of oedema, as described by Lin et al. (1993). It was calculated by subtracting the area of non-infarcted ipsilateral isocortex from the area of contralateral isocortex, taking the number of intervals and the thickness of sections into account (180 μm). The following formula was used: Infarct volume = [(area of contralateral isocortex × d) – (area of ipsilateral non-infarcted isocortex × d)] where d is distance between each section. All imaging and image analysis were performed by blinded investigators.

Immunofluorescence microscopy

Sections were immunostained as follows: 1 h incubation with a blocking solution consisting of 10% normal donkey serum (NDS), 1% bovine serum albumin (BSA), 0.5% Triton X-100 in 0.01 M phosphate-buffered saline (PBS). The sections were incubated overnight with primary antibodies diluted in 3% NDS, 1% BSA, 0.5% Triton X-100 in 0.01 M PBS. Sections were washed in PBS and incubated with secondary antibodies in 3% NDS, 1% BSA in 0.01 M PBS for 1 h. A list of all primary and secondary antibodies used for immunofluorescence experiments is provided in Table 3. Nuclei were stained by 5 min incubation with 1:5000 Hoechst 33 258 (Thermo Fisher Scientific cat. no. H3569, RRID:AB_2 651 133) diluted in PBS. Finally, sections were mounted using ProLong Gold antifade reagent (Thermo Fisher Scientific; cat. no.: P36934; RRID:SCR_01 5961) and dried overnight.

Quantitative analysis of GFAP and lipocalin-2 immunoreactivity and astrocyte process density

Images from WT (n = 8), AQP4$^{+/-}$ (n = 7) and AQP4 (n = 7) mice subjected to dMCAO were acquired with a Zeiss 710 LSM for GFAP intensity and 780 LSM for lipocalin-2 (LCN2) LCN2 intensity analysis (Carl Zeiss Microscopy) with a ×10 air objective. All images were taken from the isocortex, superior to the infarction.

Analysis was conducted by investigators blinded to the genotypes of the animals utilizing ZEN blue 3.2 (Carl Zeiss Microscopy).

Astrocyte process density was recorded along a line spanning the edge of the infarct zone. Signals above 1.5 times the background median GFAP or LCN2 expression were identified as peaks if they were the highest signal within a 3 μm range. Peaks were ordered by GFAP or LCN2 intensity, and an arbitrary cut-off at the top 75th

percentile was introduced to permit us to differentiate between thicker processes and thinner ones.

For GFAP intensity profiles, regions of interest (ROI) were defined as a rectangle 300 μm wide and 600 μm long starting at the edge of infarction. The ROI was centred on the halfway point between the white matter and the surface of the cortex. The linear profile was extracted from each ROI, with the 0 μm mark on the edge of infarction, and 600 μm mark distal to the infarction. Intensity values were extracted with ZEN blue version 1.1.2.0 (Carl Zeiss Microscopy, 2012).

Visual inspection of the raw graphs revealed that the 500–600 μm range had flattened out. Median values from this region were used to represent a baseline ipsilateral astrogliosis and subtracted from the raw values of the entire 0–600 μm range. The median subtracted values were subjected to locally weighted scatterplot smoothing (LOWESS) regression (broadband set to 0.1) using Stata 17 (Statacorp, College Station, TX, USA) to smooth out the graphs and allow for comparison of local averages. The resulting graph shows the 'hyper reactive' zone of astrogliosis, proximal to the infarction, above baseline ipsilateral GFAP expression. LOWESS graphs from all animals showed a similar pattern with a plateau at the 25–325 μm area, followed by a gradual decline from 325 to 500 μm away from the infarction. Area under curve (AUC) values for these regions, as well as the total 0–600 μm and 500–600 μm regions were compared between groups.

For LCN2 analysis Qupath verson 5.0 (Bankhead et al., 2017) was used to conduct an object based colocalization. ROIs were defined as 300 μm and 200 μm tall polygons starting on the edge of the infarct core visualized by GFAP staining. All ROIs were made to be 60,000 μm^2 to ensure equal sampling despite differences in ROI shape. Using the pixel classification tool each ROI was segmented using a set GFAP intensity threshold of 1000 with Gaussian smoothing of 1. The LCN2 mean intensity per μm^2 and total intensity of LCN2 in the GFAP positive segment of the ROI were compared between groups.

Microglia quantification

Z-stacks (25 images spanning 12 μm) were captured from WT ($n = 9$), AQP4$^{+/-}$ ($n = 9$), and AQP4$^{-/-}$ ($n = 9$) mice using a Zeiss 710 LSM. For each animal four ROIs were defined: the molecular layer and the external pyramidal layer of the isocortex from both ipsilateral and contralateral hemispheres. The ROIs in the ipsilateral hemisphere were 500 μm away from the infarct core, on its superior side (Fig. 4*A*).

Microglia quantification was performed using Trainable Weka Segmentation plugin (release v3.1.2) (Arganda-Carreras et al., 2017) on ImageJ. Ten stacks starting from where the entire captured frame is visibly labelled were acquired for the quantification. A maximum intensity of stacks was created using Carl Zeiss ZEN 2.3 SP1 (black, 64bit, release version 14) and exported in TIFF format prior to quantitative analysis on ImageJ.

For the quantification, images were saved with one channel showing IBA1 labelling to avoid large nuclei of neurons, after particle size filtration, to be counted as microglia. After opening the images in ImageJ and setting the scale (Analyse > Set scale), the Trainable Weka Segmentation plugin was called (Plugin > Segmentation > Trainable Weka Segmentation). Training was performed by defining two classes, background and microglia. After completion of training, classifier and data were saved to use in all the images. The result was created and saved as TIFF format. The images were converted to 8-bit (Image > Type > 8-bit). After setting the threshold on auto (Image > Adjust > Threshold > Auto), a mask was created (Process > Binary > Convert to mask). Five and 10 μm^2 were used as a lower bound for particle size before measuring the area covered by microglia and count respectively. The area covered by microglia was measured by command Analyse > Measure. Microglia quantification was calculated by command Analyse > Analyse Particles. To control for the accurate number of microglia where microglia processes overlapped and the software was not able to distinguish them as separate cells, original z-stack images were used to manually check that. Microglia cells with the soma touching the edges of the images were excluded from the microglia quantification.

M1/M2 microglia imaging and analysis

For the M1-marker iNOS, whole sections from WT ($n = 10$), AQP4$^{+/-}$ ($n = 9$), and AQP4$^{-/-}$ ($n = 9$) mice were scanned using AxioScan Z1 (Carl Zeiss Microscopy) with ×20 objective. For each section three planes were captured, and the best was used for quantification. For M1-marker CD16/32 (WT $n = 6$, AQP4$^{+/-}$ $n = 6$, and AQP4$^{-/-}$ $n = 6$), M2-markers CD206 (WT $n = 6$, AQP4$^{+/-}$ $n = 7$, and AQP4$^{-/-}$ $n = 7$), and Arg1 (WT $n = 5$, AQP4$^{+/-}$ $n = 7$, and AQP4$^{-/-}$ $n = 6$), whole sections were scanned in a single plane using a VS200 Slide Scanner (Olympus, Tokyo, Japan). Analyses were conducted by investigators blinded to the genotype of the animals in the following manner. Images were annotated using QuPath (Bankhead et al., 2017) and ROIs were defined as follows. First, the ipsilateral ROI starts 250 μm away from the infarct core, and spans 500 μm wide and the entire depth of the cortex. The contralateral ROI is of equivalent size and anatomical location to the ipsilateral

ROI. The Core ROI spans most of the ischaemic core without obvious tearing or artefacts.

Stardist (Schmidt et al., 2018), open source machine learning software, was used to detect nuclei. Cells were defined as a 1 μm expansion of the detected nuclei. To avoid interarea and intersection variability confounding positive cell detections, custom object classifiers were trained using the artificial neuronal network module in QuPath. The training was conducted as human-in-the-loop until the classifiers were satisfactory. Two values were used for comparison between genotypes: first the ratio of IBA^{+} and iNOS/CD16-32/Arg1/CD206^{+} double positive cells to total IBA^{+} cells in each ROI; and second, the number of

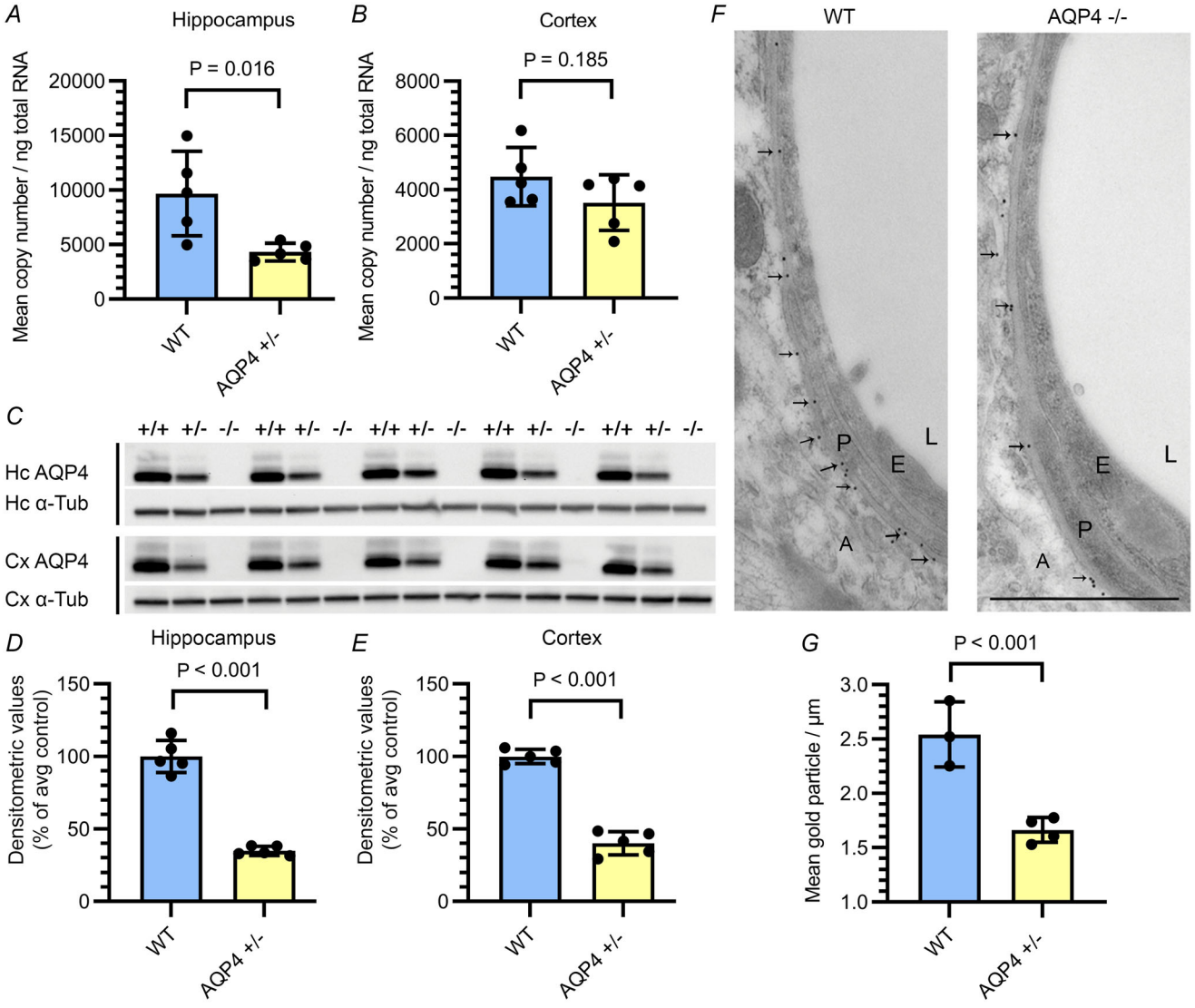

Figure 1. AQP4$^{+/-}$ mice exhibit reduced expression of Aqp4 transcripts, protein and perivascular AQP4 localization

A and *B*, RT-qPCR analysis of parietal cortex and hippocampus of WT and AQP4$^{+/-}$ mice. Bar graphs show the copy numbers per nanogram of Aqp4. No significant decrease was found in AQP4$^{+/-}$ samples compared to WT in parietal cortex (*A*). In AQP4$^{+/-}$ hippocampus, there was a significant 56% decrease of Aqp4 transcripts compared to WT (*B*). $n = 5$ for AQP4$^{+/-}$ and $n = 5$ for WT; error bars indicate mean with SD. *C*–*E*, representative immunoblots and quantification expressed as a percentage of average control values of total protein lysates from hippocampus and parietal cortex of WT and AQP4$^{+/-}$ mice. α-Tubulin was used as the loading control (*C*). A significant decrease in AQP4 protein expression in AQP4$^{+/-}$ *vs*. WT was observed in each region according to an independent samples *t* test, 65% in hippocampus (*D*) and 60% in parietal cortex (*E*). $n = 5$ for each genotype; bars show mean and SD. *F* and *G*, quantitative immunogold analysis of perivascular AQP4 in parietal cortex. The AQP4 mean linear density in cortex AQP4$^{+/-}$ (median 1.38) is significantly lower than the linear density of WT. Error bars 95% CI and mean. $n = 3$ for WT and $n = 4$ for AQP4$^{+/-}$.

IBA$^+$ and iNOS/CD16-32/Arg1/CD206$^+$ double positive cells divided by total number of cells in each ROI to normalize for variation between ROIs.

Statistical analysis

For analysis of RT-qPCR, the mean copy number per ng of total cDNA input was compared between genotypes. For analysis of western blotting, values are shown as a percentage of mean WT values. The data was analysed by independent samples Student's *t* test in SPSS Statistics Version 25 (IBM Corp., Armonk, NY, USA).

The data from immunogold electron microscopy quantification was exported to SPSS version 25 for further statistical analysis. Significance was determined by non-parametric Mann–Whitney *U* test.

The volumetric data for infarct volume calculation was exported to SPSS. Natural log transformed data were subjected to one-way ANOVA with LSD *post hoc* test.

For analysis of GFAP and LCN2 immunoreactivity and astrocyte process density, all measurements for each animal were normalized to the infarct volume, before conducting statistical analysis in Stata 17. The data were lognormally distributed, and hypothesis testing was done on log-transformed values with one-way ANOVA.

The data from microglial count and area coverage were exported to SPSS, and statistical analysis was performed by non-parametric Mann-Whitney *U* test.

The data from M1/M2 microglia analysis was assessed for normal distribution using the Shapiro–Wilk test QQ-plots and histograms. One-way ANOVA was conducted to compare the genotypes for each ROI on raw or log-transformed values where appropriate.

For all analyses, data are presented as mean values ± SD, and $P < 0.05$ was considered as significant.

Results

AQP4$^{+/-}$ mice exhibit reduced level of *Aqp4* transcripts and decreased AQP4 expression in perivascular membrane domains

The RT-qPCR analysis revealed a regional heterogeneity in expression of *Aqp4* transcripts in AQP4$^{+/-}$ animals compared to WT (Fig. 1*A* and *B*). No significant decrease was found in AQP4$^{+/-}$ samples compared to WT in parietal cortex (mean WT 4481, mean AQP4$^{+/-}$ 3561, independent samples *t* test, $P = 0.185$). In hippocampus, there was a significant decrease (by 56%) of *Aqp4* transcripts in *Aqp4*$^{+/-}$ mice compared to WT (mean WT 9679, mean AQP4$^{+/-}$ 4325, independent samples *t* test, $P = 0.016$).

When investigating AQP4 total protein expression from different regions, we found that AQP4 was decreased in AQP4$^{+/-}$ mice (Fig. 1*C*). AQP4 expression was reduced by ∼65% in hippocampus and by ∼60% in parietal cortex (hippocampus: total AQP4 mean WT = 100, mean AQP4$^{+/-}$ = 34.94, independent samples *t* test, $F = 5.084$ sig. = 0.054, sig. 2-tailed = 0.000; parietal cortex: mean WT = 100, mean AQP4$^{+/-}$ = 40.14, independent samples *t* test, $F = 1.907$ sig. = 0.205, sig. 2-tailed = 0.000) (Fig. 1*D* and *E*).

We performed quantitative immunogold electron microscopy to assess the expression of AQP4 in astrocytic perivascular membrane domains (Fig. 1*F*). We found that the linear density of AQP4 protein around capillaries of AQP4$^{+/-}$ mice was reduced by 35% compared to WT (parietal cortex, Fig. 1*G*). The linear density of AQP4 immunogold particles was 1.38 per μm membrane in AQP4$^{+/-}$ animals compared to 2.34 in WT ($P < 0.001$).

Partial or total deletion of AQP4 does not impact IBA1 or GFAP protein expression in control mice

To assess whether partial or total deletion of AQP4 has an impact on astrocyte or microglia activity under basal conditions, we analysed expression of Iba1 (microglia marker) and GFAP (astrocyte marker) (Fig. 2*A*). Immunoblot analysis of total protein expression of Iba1 and GFAP in parietal cortex of WT, AQP4$^{+/-}$, and

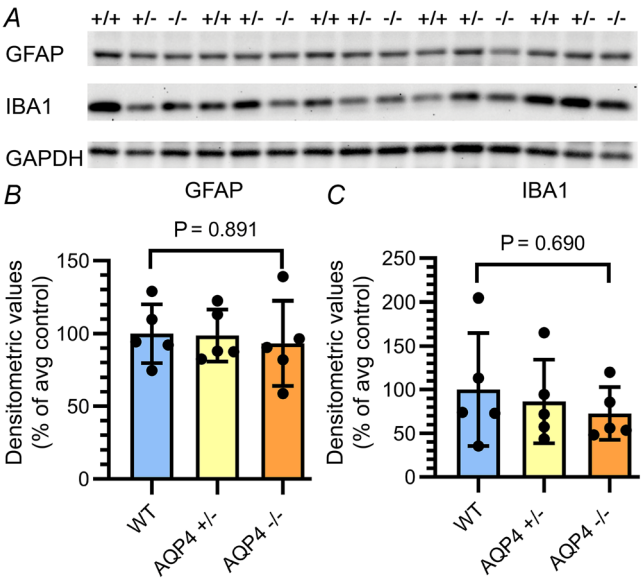

Figure 2. No differences observed in GFAP and IBA1 protein levels among the genotypes under basic conditions
Representative immunoblot (*A*) and quantitation (*B* and *C*) expressed as a percentage of average control values of total protein lysates from parietal cortex of WT, AQP4$^{+/-}$ and AQP4$^{-/-}$ mice.GAPDH was used as the loading control. No significant decrease in IBA1 or GFAP expression between genotypes was observed. *n* = 5 for each genotype; bars shown mean and SD.

$AQP4^{-/-}$ mice, showed no significant difference between the genotypes (Fig. 2*B* and *C*).

Infarct volume is decreased in $AQP4^{-/-}$ mice subjected to dMCAO

As expected, dMCAO induced discrete infarcts limited to the ipsilateral cortex (Fig. 3*A*) (Doyle & Buckwalter, 2014). The lesion was evaluated with Cresyl Violet staining and calculated as described in the Methods section (Fig. 3*B*).

In $AQP4^{-/-}$ mice the infarct volume after dMCAO occlusion was 49% of the infarct volume in WT littermates ($P = 0.034$). The infarct volume was 5.472 ± 2.306 mm^3 in $AQP4^{-/-}$, 11.19 ± 6.903 mm^3 in WT compared to 9.048 ± 2.306 mm^3 in $AQP4^{+/-}$ mice. The infarct volume in the $AQP4^{+/-}$ did not differ significantly from the infarct volume of the two other genotypes (Fig. 3*C* and *D*).

Partial or complete deletion of AQP4 does not lead to any changes in the number or areal fraction of microglia in mice subjected to dMCAO occlusion

While microglia have ramified morphology with thin processes in their 'resting' state, they develop larger

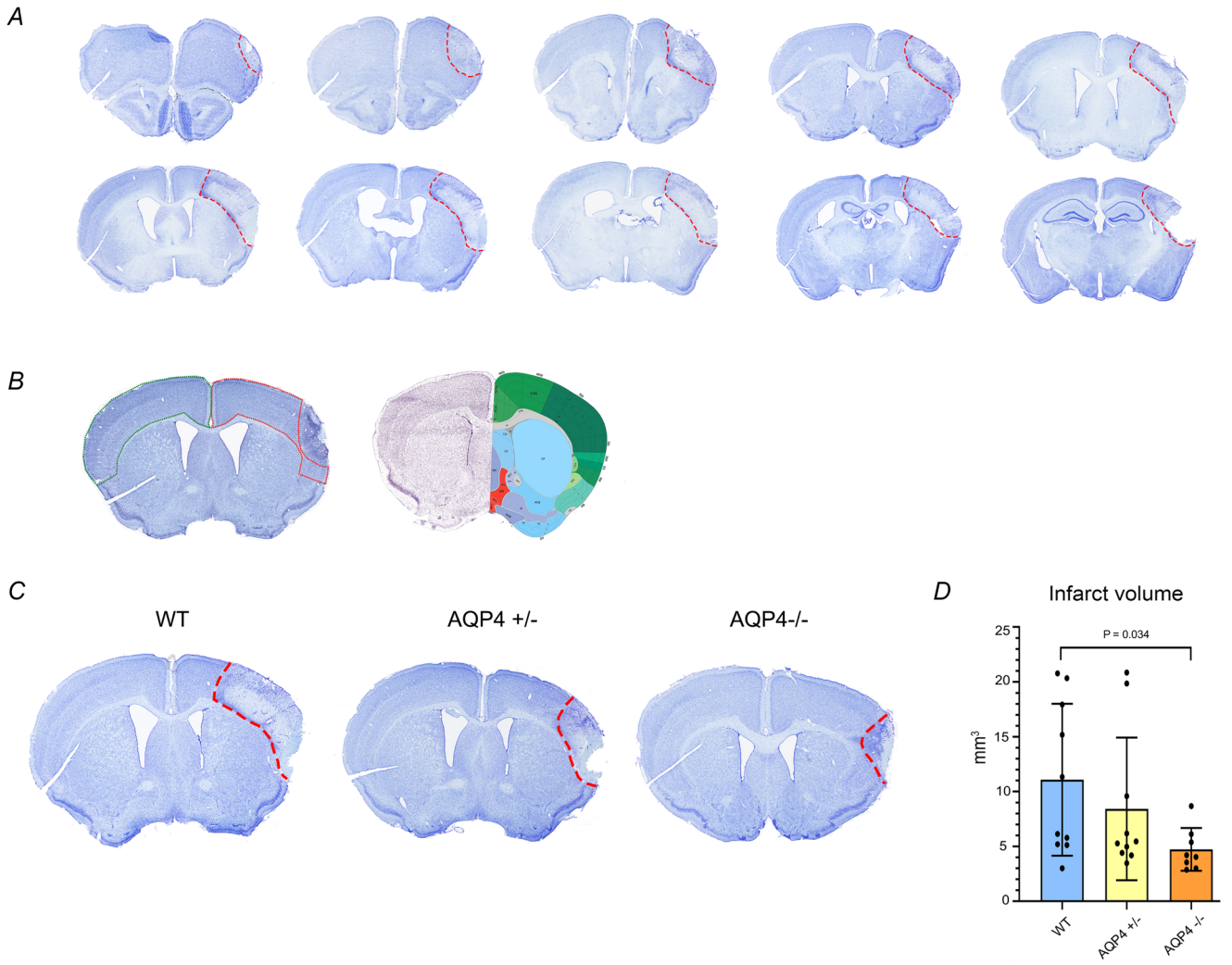

Figure 3. Volumetric analysis shows signficantly lower infarct volume in $AQP4^{-/-}$ mice
A, representative Cresyl Violet stained coronal brain sections used for volumetric analysis. Dashed red lines show infarcted tissue. *B*, representative image (left) of a Cresyl Violet stained coronal brain section 7 days after dMCAO. The green line indicates selection of isocortex, with Allen Brain Atlas overlay on the right (Allen Institute for Brain Science, 2004) of the contralateral hemisphere and the red line shows the non-infarcted isocortex of the ipsilateral brain. The pale area in the right hemisphere displays the infarcted area. *C*, representative Cresyl Violet stained sections from WT, $AQP4^{+/-}$, and $AQP4^{-/-}$ animals. Infarcted area marked with dashed lines. *D*, bar graph showing statistical analysis of the infarct volume. Infarct volume in $AQP4^{-/-}$ mice is significantly lower compared with WT, 7 days after dMCAO. The infarct volume in $AQP4^{+/-}$ mice is not statistically different from the infarct volume in WT and $AQP4^{-/-}$ mice. Bars show mean and SD.

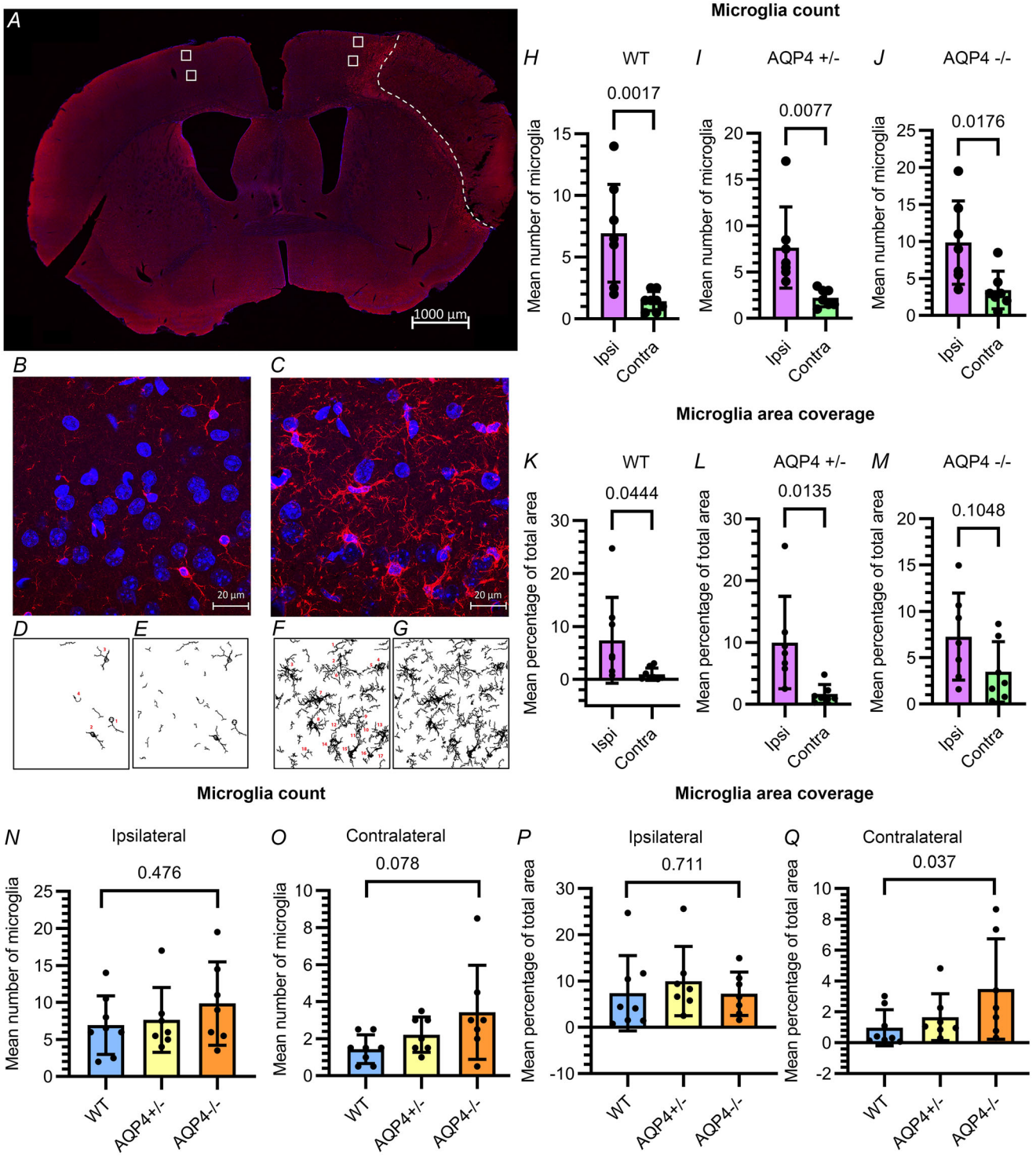

Figure 4. Total number and fraction of total area covered by microglia in the peri-infarct area and contralateral cortex of WT, AQP4$^{+/-}$ and AQP4$^{-/-}$ mice

A, representative immunofluorescent stained coronal brain section 1 week after dMCAO, depicting the regions of interest for imaging in the peri-infarct area and the corresponding area in the contralateral cortex. The regions from the peri-infarct area were obtained at 500 μm distance from the infarct border (shown with dashed line) to quantify the total microglia coverage and count. *B* and *C*, representative ×63 confocal image from contralateral (*B*) and ipsilateral (*C*) isocortex of immunofluorescent stained brain section with nuclear stain in blue and antibody against IBA1 in red. *D*–*G*, illustration of the created masks from *B* and *C* for quantification of microglia number (*D* and *F*)

and the total area covered by microglia (*E* and *G*) in the contralateral and ipsilateral isocortex, respectively. *H–J*, mean number of microglia in each ROI is significantly higher in the peri-infarct area compared to corresponding areas in the contralateral isocortex of all three genotypes. *K–M*, mean fraction of total area covered by microglia is significantly higher in the peri-infarct area of WT and AQP4$^{+/-}$ but not AQP4$^{-/-}$. *P* and *Q*, there is no significant difference between the three genotypes in the mean number of microglia per ROI in ipsilateral and contralateral isocortex. The area fraction of microglia in the contralateral but not ipsilateral isocortex is significantly higher in AQP4$^{-/-}$ mice compared to that of WT mice. Bars show mean and SD.

somata and thicker processes when 'activated' (Lier et al., 2021). As a result activated microglia cover a larger areal fraction than they do in their resting state. To investigate microglial activation, area-fraction analysis was performed (Fig. 4). Moreover, we quantified the number of microglia in smaller ROIs adjacent to the infarct in the ipsilateral isocortex and in corresponding areas in the contralateral isocortex of WT, AQP4$^{+/-}$ and AQP4$^{-/-}$ mice (Fig. 4*A–G*).

Our quantitative data show that the number of microglia, assessed by IBA1 immunostaining, is significantly higher in the ipsilateral isocortex compared to the contralateral side in all genotypes (WT ($P = 0.001$), AQP4$^{+/-}$ ($P = 0.007$) and AQP4$^{-/-}$ ($P = 0.017$) (Fig. 4*H–J*). The area fraction covered by microglia is significantly higher in the ipsilateral isocortex compared to the contralateral side of AQP4$^{+/-}$ ($P = 0.0135$) and WT ($P = 0.044$) but not in AQP4$^{-/-}$ ($P = 0.1048$) (Fig. 4*K–M*).

Our analysis further shows no significant differences in the number of microglia between the genotypes (Fig. 4*N*, *O*), and areal fraction covered by microglia in the ipsilateral isocortex adjacent to the infarct (Fig. 4*P*). However, the areal fraction covered by microglia in the contralateral isocortex is significantly higher in the AQP4$^{-/-}$ mice compared to the WT ($P = 0.0139$) (Fig. 4*Q*).

After a stroke, microglia can assume different activation states, including the pro-inflammatory M1 phenotype and the anti-inflammatory M2 phenotype (Jiang et al., 2020). To assess whether partial or total deletion of IBA1 AQP4 has an impact on polarization of microglia into M1 or M2 phenotypes, we analysed the cell density of total stained microglia, and the ratio of M1 microglia (double stained IBA1-iNOS or IBA1-CD16/32) and M2 microglia (double stained IBA1-CD206 or IBA1-Arginase-1) to total microglia in infarct core or the ipsilateral border, and contralateral isocortex of the three genotypes (Fig. 5*A–T*). Our analyses showed no significant differences in total density of IBA1-stained microglia in any of the regions of the three genotypes (Fig. 5*B–D*). Furthermore, no differences were found between the three genotypes in the infarct core or ipsilateral border for any M1 or M2 markers and in the contralateral cortex for three of the markers (Fig. 5*I–S*). The only significant difference was in the CD206 (M2 marker) density, which was significantly lower in the contralateral isocortex of the AQP4$^{-/-}$ mice compared to WT (Fig. 5*T*).

A complete loss of AQP4 increases GFAP intensity in the peri-infarct zone but leaves the astrocytic process density unchanged

The astrocytic process density was measured along the infarct border using GFAP immunofluorescence (Fig. 6*A* and *B*). In addition to all immunofluorescence peaks that met the criteria (see Methods), the 75th percentile peaks (representing the larger astrocyte branches) were counted. All animals showed the glial scar forming phenotype of astrocytic processes oriented towards the infarct. No difference was found when comparing the astrocyte process density between genotypes ($P = 0.356$ for all peaks, $P = 0.448$ for 75th percentile peaks) (Fig. 6*C* and *D*).

The second measurement was the area under curve (AUC) of GFAP expression with the *x*-axis starting on the infarct border and moving distally (Fig. 6*E–G*). This allowed us to identify a hyper-reactive plateau approximately 300 μm long expressing more GFAP than the general astrogliosis seen in the ipsilateral cortex (Fig. 6*H*). This plateau was present for all genotypes close to the infarction in the 25–325 μm range, and is interpreted as the beginning glial scar (Bardehle et al., 2013). Following the plateau is a steady decline in GFAP intensity (Fig. 6*H*).

When comparing genotypes, the glial scar forming area has a significantly higher ($P = 0.035$) expression of GFAP in AQP4$^{-/-}$ (155,437.6 ± 150,720.1) compared to AQP4$^{+/-}$ (63,663.39 ± 37,277.16) and WT (55,591.53 ± 37,814.13) (Fig. 6*J*). Interestingly, the WT and AQP4$^{+/-}$ had similar values, indicating that a total loss of AQP4 is responsible for the increased GFAP expression and astrogliosis. No difference was found in the other regions examined (Fig. 6*I*, *K* and *L*), thus making the increase in GFAP expression in AQP4$^{-/-}$ specific to the glial scar forming area.

Immunofluorescence analysis of LCN2, a marker of astroglial reactivity, revealed staining in a subset of GFAP-positive reactive astrocytes located adjacent to the infarct border in all three experimental groups (Fig. 6*M–P*). Occasional faint LCN2 staining was also observed in GFAP-positive astrocytes situated farther away from the infarct border in the ipsilateral cortex or the contralateral cortex. The staining intensity of LCN2 in GFAP-positive astroglial processes at the infarct border was assessed (Fig. 6*Q* and *R*). No significant differences

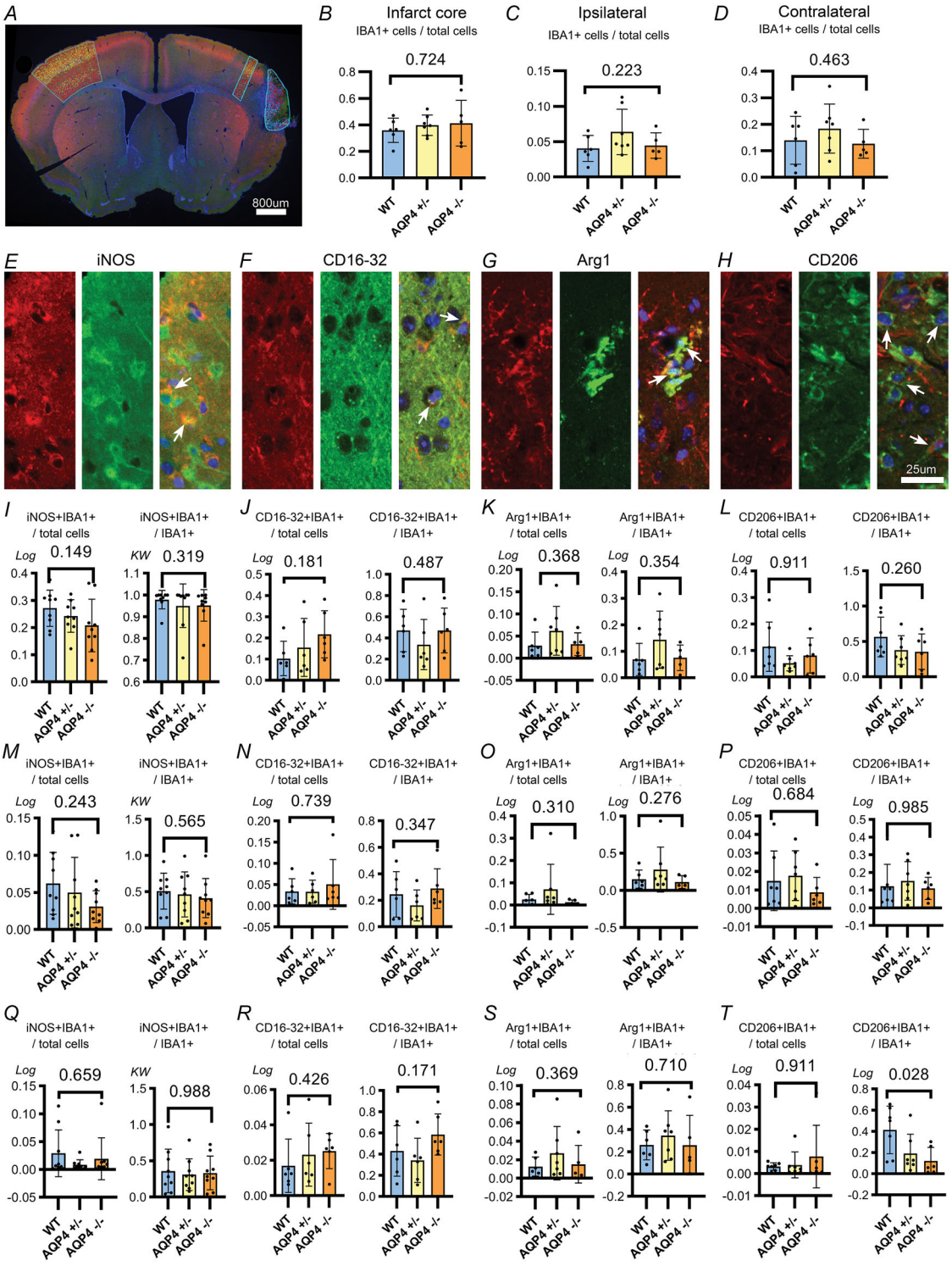

Figure 5. No difference in total density of IBA1-stained microglia or M1/M2 markers in any of the regions of the three genotypes

A, representative immunofluorescent stained coronal brain section 1 week after dMCAO, with annotated regions of interest containing cell detection overlays. *B–D*, number of IBA1 positive cells divided by total cells detected for each ROI. No significant difference was detected when comparing genotypes. *E–H*, representative confocal images from ipsilateral cortex for each experiment showing colocalization between IBA1 (pseudocolour red) and the respective marker (pseudocolour green). Rightmost panel also contains nuclear stain (pseudocolour blue). *I–L*, quantification of infarct core ROI; *M–P*, quantification of ipsilateral ROI; and *Q–T*, quantification of contralateral

ROI. *I–T*, left graph depicts number of double positive cells divided by total cells detected in the ROI. These values indicate changes in the number of double positive cells. Right graph depicts number of double positive cells divided by total IBA1 positive cells in the ROI to show the proportion of microglia positive for the respective marker. All graphs show non-transformed values, *E*, *I*, *M* and *Q* show images and graphs regarding iNOS positive microglia, *F*, *J*, *N* and *R* for CD16-32 positive microglia, *G*, *K*, *O* and *S* for Arg1 positive microglia, and *H*, *L*, *P* and *T* for CD206 positive microglia. Arrows show IBA1 and marker positive cells. Bars show mean and SD. *P*-values are presented above each bar graph.

were found in the LCN2 intensity per total peri-infarct area or in the GFAP-positive processes between the genotypes (Fig. 6*S* and *T*).

Discussion

Previous studies of AQP4 have focused on investigating the role of AQP4 in the development and resolution of oedema, particularly in the context of middle cerebral artery occlusion (MCAO), which results in the formation of a large oedema accompanied by cortical and striatal infarction (Amiry-Moghaddam et al., 2003; Frydenlund et al., 2006; Hirt et al., 2017; Manley et al., 2000; Yao et al., 2015).

The objective of the present study was to examine the impact of AQP4 on infarct volume and the peri-infarct zone beyond its established role in oedema. To accomplish this, we employed an experimental model of distal middle cerebral artery occlusion (dMCA, which induces smaller infarcts than MCAO and less oedema (Doyle & Buckwalter, 2014).

Our study revealed that AQP4$^{-/-}$ mice demonstrate a significant reduction in infarct volume 1 week after dMCAO compared to wild-type mice. This indicates that the absence of AQP4 confers a protective effect against ischaemic brain damage, in addition to its established role in oedema development. In mice with hemizygous deletion of AQP4 (AQP4$^{+/-}$), the infarct volume was not significantly different from wild-type.

We hypothesized that the reduced infarct size observed in AQP4$^{-/-}$ mice following experimental stroke could be attributed to AQP4-dependent changes in the peri-infarct zone. Specifically, we assessed whether AQP4 deletion led to altered patterns of astrocyte or microglial activation in this zone. Recent research shows that the absence of AQP4 leads to a strong reduction in microglial activation after intrastriatal injection of 1-methyl-4-phenylpyridinium (Prydz et al., 2020).

Our data showed an increased intensity of GFAP, indicating heightened astrocyte reactivity, in the peri-infarct zone of AQP4$^{-/-}$ mice. Astrocytes respond to ischaemic insults by undergoing increased proliferation, hypertrophy and elevated GFAP expression. Multiple lines of evidence indicate that these reactive astrocytic responses are crucial in limiting the size of the ischaemic core and contribute to the improvement of stroke outcomes (Choudhury & Ding, 2016). A previous study revealed that 7 days after MCA transection, the infarct volume was 210% to 350% higher in GFAP$^{-/-}$Vim$^{-/-}$ mice compared to WT mice (Li et al., 2008). The elevated GFAP expression in our study signifies astrocyte activation and suggests the potential involvement of astrocytes in the protective mechanisms associated with AQP4 deficiency. However, the deletion of *Aqp4* did not exert a similar impact on the LCN2 intensity, another marker of reactive gliosis, as no discernible differences were observed between the genotypes. LCN2 serves as a marker of reactive astrogliosis and has been linked to various acute CNS injuries, including stroke (Lee et al., 2009; Suk, 2016). Multiple lines of evidence suggest that LCN2, when secreted by reactive astrocytes, exerts a pro-inflammatory and neurotoxic effect. Mice lacking LCN2 due to genetic deletion exhibit reduced infarct volume and neuroinflammation following transient MCAO (Jin et al., 2014). In our study, LCN2 expression was detected in a limited number of astrocytes proximal to the infarct core. Of note, peak expression of LCN2 occurs 24 h post-stroke, while our study harvested brains at 7 days post-stroke. Nevertheless, an increased GFAP intensity in AQP4$^{-/-}$ mice in the absence of a concurrent elevation in LCN2 levels is consistent with a net protective effect of *Aqp4* deletion. The detailed mechanisms will be explored in forthcoming investigations.

Microglia, the resident immune cells of the CNS, play a critical role in the neuroinflammatory response that occurs after a stroke (Xiong et al., 2016). These cells can assume different activation states, including the pro-inflammatory M1 phenotype and the anti-inflammatory M2 phenotype (Jiang et al., 2020). We did not observe any difference between the three genotypes in the number of microglia, nor the M1 and M2 subtypes in the infarct core and the border zone. The subtle differences we observed were in the neocortex areas contralateral to the infarct, which cannot explain the lower the infarct volume in the AQP4$^{-/-}$ mice. Our findings are in contrast to another study by Hirt et al. (2017) which showed a significantly weaker IBA1 staining in the peri-infarct area of AQP4$^{-/-}$ mice, 14 days after transient MCAO. In our study the mice were subjected to permanent dMCAO, which leads to a smaller lesion size and oedema formation than transient MCAO used by Hirt et al. Moreover, our analyses were done on day 7 after the onset of ischaemia. Both the model used and the time after stroke may explain the discrepancy observed

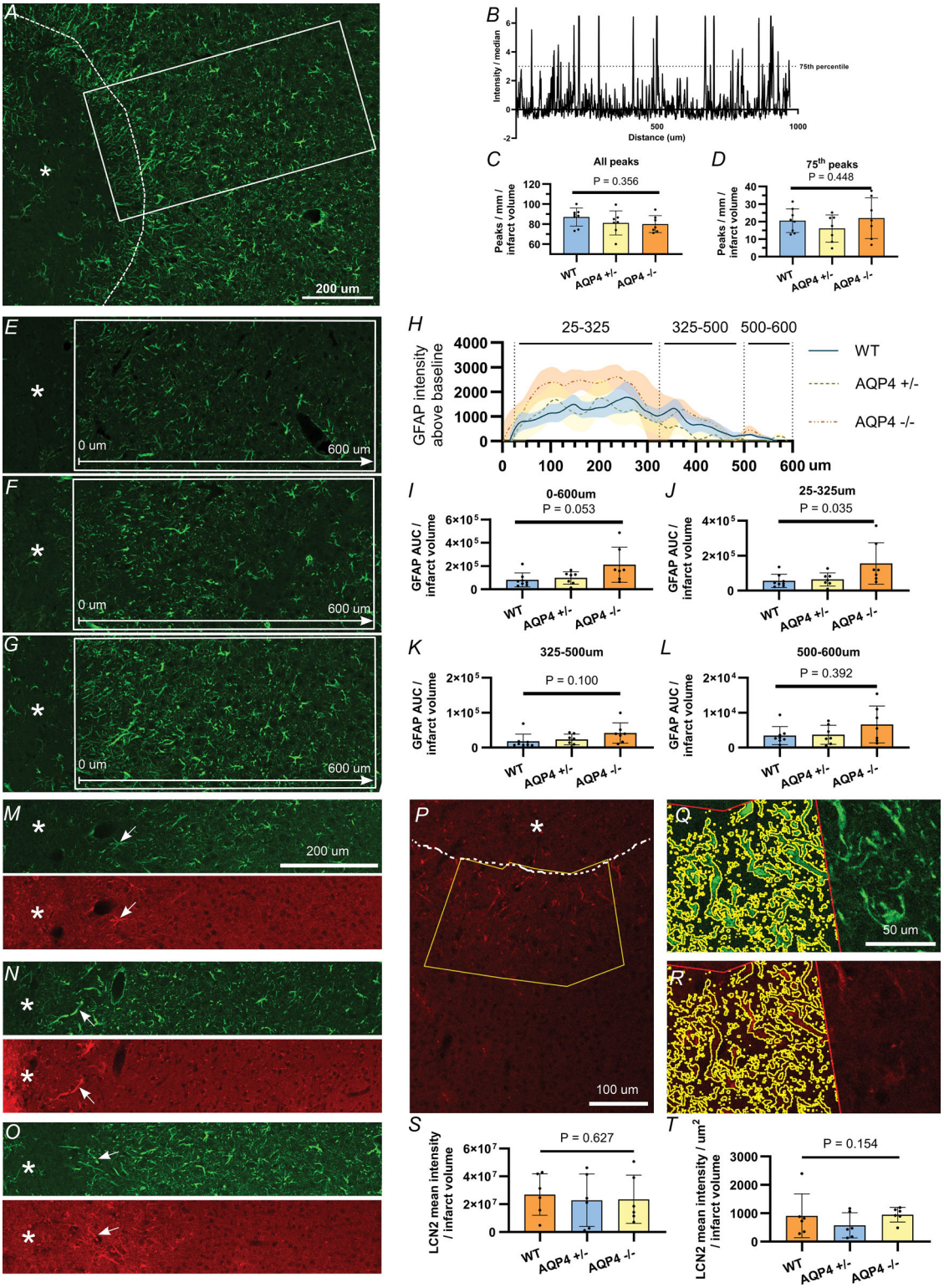

Figure 6. Significantly higher GFAP intensity in the peri-infarct zone of AQP4$^{-/-}$ mice compared to the WT

A, section incubated with anti-GFAP antibody shows astrogliosis at the infarct border. The image is taken from the superior infarct border and the rectangular ROI for the analysis of astrogliosis (GFAP immunoreactivity) is shown. Dashed line shows linear profile used for astrocyte process density analysis. *B*, LOWESS graph from linear density ROI with 75th percentile threshold, showing the intensity of the GFAP^{+} processes crossed by the dashed line. *C* and *D*, graph showing quantification of all peaks (*C*) and 75th percentile peaks (*D*) in different genotypes. No

significant difference was found between the genotypes. *E–G*, representative ROIs from wild-type (*E*), AQP4$^{+/-}$ (*F*), and AQP4$^{-/-}$ (*G*) brain sections showing GFAP immunoreactivity along a line starting at the infarct border and extending 600 um away. The labelling intensity along this line was measured and used for the GFAP immunoreactivity analysis. *H*, mean and SEM for LOWESS graphs grouped by genotype. Mean shown by line and SEM shown by hue. Blue continuous line shows wild type, red dashed line shows AQP4$^{+/-}$, and green dashed line shows the mean GFAP intensity in AQP4$^{-/-}$. *I–K*, area under curve quantification for the entire graph (*I*), for the 25–325 μm range (*J*) and for the 325–500 μm range (*K*) are compared between the genotypes. The values were significantly higher for the AQP4$^{-/-}$ group compared to the WT and AQP4$^{+/-}$ groups in the 25–325 μm range. The values for each animal were normalized for the infarct volume. *L*, area under curve quantification for the 500–600 μm tail end used to subtract ipsilateral baseline GFAP immunoreactivity. *M–O*, representative images showing immunolabelling for GFAP (green) and LCN2 (red) in wild-type (*M*), AQP4$^{+/-}$ (*N*), and AQP4$^{-/-}$ mice (*O*). Arrows show astrocyte processes co-stained with both LCN2 and GFAP. *P*, placement of 300 μm wide and 200 μm deep ROI for LCN2 quantification at the edge of infarction marked by yellow line. Astrocytic LCN2 is only found in reactive astrocytes adjacent to the infarct border indicated by the white dashed line. *Q* and *R*, yellow segmentation based on GFAP immunostaining (*Q*) which is used for quantification of LCN2 immunolabeling (*R*) intensity in astrocyte processes. *S* and *T*, bar graphs showing quantification of total LCN2 labelling intensity in GFAP segment (*S*) and LCN2 labelling in the total ROI area (*T*). The values were normalized for infarct volume. No difference was found between groups. GFAP immunostaining (pseudocolour green), LCN2 immunostaining (pseudocolour red). Asterisk indicates the infarct core. *E–G*, region of interest (ROI) is 600 μm long and 200 μm wide. *C* and *D*, *I–L*, and *S* and *T*, bar graphs display individual non-transformed values as dots, with mean and standard deviation for each group. The *P*-values from one-way ANOVA on log-transformed values are presented above the columns. Scale bars: 200 μm (*A*, *M–O*), 100 μm (*P*), 50 μm (*Q* and *R*).

in the two studies. Taken together, our findings show that deletion of AQP4 significantly reduces infarct size in a stroke model that produces discrete infarcts confined to the cortex. Deletion of AQP4 also leads to discrete changes in the peri-infarct zone, most notably to an activation of astrocytes in the infarct-near part of this zone. While reactive astrocytes have been proposed to play a protective role in cerebral ischaemia (Williamson et al., 2021), further studies are required to establish whether or how the observed astrocyte activation contributes to restricting infarct size after AQP4 deletion. A complete or near-complete loss of AQP4 seems to be required for a protective effect to occur, as a partial deletion of AQP4 did not produce any significant effects on infarct size.

The aim of our study was to use the dMCAO model to assess the impact of AQP4 on infarct volume and the infarct border zone, distinct from its established role in oedema formation. The dMCAO model offers a significant advance over the conventional MCAO model, which typically results in a fulminant oedema confounding the effects on infarct formation. Our study has limitations. Thus, even dMCAO induces a modest oedema, and the craniotomy itself can lead to some oedema formation and disruption of the blood–brain barrier (Liu et al., 2022). Therefore, we cannot dismiss the possibility that the oedema in this model may contribute, at least partially, to the infarct volume. This limitation notwithstanding, we hold that the present study using the dMCAO model has helped us disentangle the effects of AQP4 on oedema formation from the effects of AQP4 on the infarct itself. Future studies are required to unveil the detailed mechanisms underlying the protective effect of *Aqp4* deletion and to test our hypothesis that this effect is coupled to astroglial activation in the infarct border zone.

References

Allen Institute for Brain Science (2004). Allen Mouse Brain Atlas. Available from mouse.brain-map.org. Allen Institute for Brain Science (2011).

Amiry-Moghaddam, M., Frydenlund, D. S., & Ottersen, O. P. (2004). Anchoring of aquaporin-4 in brain: molecular mechanisms and implications for the physiology and pathophysiology of water transport. *Neuroscience*, **129**(4), 997–1008.

Amiry-Moghaddam, M., Otsuka, T., Hurn, P. D., Traystman, R. J., Haug, F.-M., Froehner, S. C., Adams, M. E., Neely, J. D., Agre, P., Ottersen, O. P., & Bhardwaj, A. (2003). An alpha-syntrophin-dependent pool of AQP4 in astroglial end-feet confers bidirectional water flow between blood and brain. *Proceedings of the National Academy of Sciences, USA*, **100**(4), 2106–2111.

Amiry-Moghaddam, M., & Ottersen, O. P. (2003). The molecular basis of water transport in the brain. *Nature Reviews Neuroscience*, **4**(12), 991–1001.

Arganda-Carreras, I., Kaynig, V., Rueden, C., Eliceiri, K. W., Schindelin, J., Cardona, A., & Sebastian Seung, H. (2017). Trainable Weka Segmentation: A machine learning tool for microscopy pixel classification. *Bioinformatics*, **33**(15), 2424–2426.

Banitalebi, S., Skauli, N., Geiseler, S., Ottersen, O. P., & Amiry-Moghaddam, M. (2022). Disassembly and mislocalization of AQP4 in incipient scar formation after experimental stroke. *International Journal of Molecular Sciences*, **23**(3), 1117.

Bankhead, P., Loughrey, M. B., Fernández, J. A., Dombrowski, Y., Mcart, D. G., Dunne, P. D., Mcquaid, S., Gray, R. T., Murray, L. J., Coleman, H. G., James, J. A., Salto-Tellez, M., & Hamilton, P. W. (2017). QuPath: Open source software for digital pathology image analysis. *Scientific Reports*, **7**(1), 16878.

Bardehle, S., Krüger, M., Buggenthin, F., Schwausch, J., Ninkovic, J., Clevers, H., Snippert, H. J., Theis, F. J., Meyer-Luehmann, M., Bechmann, I., Dimou, L., & Götz, M. (2013). Live imaging of astrocyte responses to acute injury reveals selective juxtavascular proliferation. *Nature Neuroscience*, **16**(5), 580–586.

Buckley, C. D., Gilroy, D. W., Serhan, C. N., Stockinger, B., & Tak, P. P. (2013). The resolution of inflammation. *Nature Reviews Immunology*, **13**(1), 59–66.

Chamorro, Á., Dirnagl, U., Urra, X., & Planas, A. M. (2016). Neuroprotection in acute stroke: Targeting excitotoxicity, oxidative and nitrosative stress, and inflammation. *Lancet Neurology*, **15**(8), 869–881.

Choudhury, G. R., & Ding, S. (2016). Reactive astrocytes and therapeutic potential in focal ischemic stroke. *Neurobiology of Disease*, **85**, 234–244.

Doyle, K. P., & Buckwalter, M. S. (2014). A mouse model of permanent focal ischemia: Distal middle cerebral artery occlusion. *Methods in Molecular Biology*, **1135**, 103–110.

Enger, R. (2017). Automated gold particle quantification of immunogold labeled micrographs. *Journal of Neuroscience Methods*, **286**, 31–37.

Frigeri, A., Gropper, M. A., Umenishi, F., Kawashima, M., Brown, D., & Verkman, A. S. (1995). Localization of MIWC and GLIP water channel homologs in neuromuscular, epithelial and glandular tissues. *Journal of Cell Science*, **108**(Pt 9), 2993–3002.

Frydenlund, D. S., Bhardwaj, A., Otsuka, T., Mylonakou, M. N., Yasumura, T., Davidson, K. G. V., Zeynalov, E., Skare, Ø., Laake, P., Haug, F.-M., Rash, J. E., Agre, P., Ottersen, O. P., & Amiry-Moghaddam, M. (2006). Temporary loss of perivascular aquaporin-4 in neocortex after transient middle cerebral artery occlusion in mice. *Proceedings of the National Academy of Sciences, USA*, **103**(36), 13532–13536.

Geiseler, S. J., Hadzic, A., Lambertus, M., Forbord, K. M., Sajedi, G., Liesz, A., & Morland, C. (2024). L-Lactate Treatment at 24 h and 48 h after Acute Experimental Stroke Is Neuroprotective via Activation of the L-Lactate Receptor HCA1. *International Journal of Molecular Sciences*, **25**(2), 1232.

Haj-Yasein, N. N., Jensen, V., Østby, I., Omholt, S. W., Voipio, J., Kaila, K., Ottersen, O. P., Hvalby, Ø., & Nagelhus, E. A. (2012). Aquaporin-4 regulates extracellular space volume dynamics during high-frequency synaptic stimulation: A gene deletion study in mouse hippocampus. *Glia*, **60**(6), 867–874.

Hirt, L., Fukuda, A. M., Ambadipudi, K., Rashid, F., Binder, D., Verkman, A., Ashwal, S., Obenaus, A., & Badaut, J. (2017). Improved long-term outcome after transient cerebral ischemia in aquaporin-4 knockout mice. *Journal of Cerebral Blood Flow and Metabolism*, **37**(1), 277–290.

Hoddevik, E. H., Khan, F. H., Rahmani, S., Ottersen, O. P., Boldt, H. B., & Amiry-Moghaddam, M. (2017). Factors determining the density of AQP4 water channel molecules at the brain-blood interface. *Brain Structure & Function*, **222**, 1753–1766.

Iadecola, C., & Anrather, J. (2011). The immunology of stroke: From mechanisms to translation. *Nature Medicine*, **17**(7), 796–808.

Iliff, J. J., Wang, M., Liao, Y., Plogg, B. A., Peng, W., Gundersen, G. A., Benveniste, H., Vates, G. E., Deane, R., Goldman, S. A., Nagelhus, E. A., & Nedergaard, M. (2012). A paravascular pathway facilitates CSF flow through the brain parenchyma and the clearance of interstitial solutes, including amyloid β. *Science Translational Medicine*, **4**(147), 147ra111.

Jiang, C. T., Wu, W. F., Deng, Y. H., & Ge, J. W. (2020). Modulators of microglia activation and polarization in ischemic stroke (Review). *Molecular Medicine Reports*, **21**, 2006–2018.

Jin, M., Kim, J.-H., Jang, E., Lee, Y. M.i, Han, H. S., Woo, D. K., Park, D. H.o, Kook, H., & Suk, K. (2014). Lipocalin-2 deficiency attenuates neuroinflammation and brain injury after transient middle cerebral artery occlusion in mice. *Journal of Cerebral Blood Flow and Metabolism*, **34**(8), 1306–1314.

Katoozi, S., Skauli, N., Rahmani, S., Camassa, L. M. A., Boldt, H. B., Ottersen, O. P., & Amiry-Moghaddam, M. (2017). Targeted deletion of Aqp4 promotes the formation of astrocytic gap junctions. *Brain Structure & Function*, **222**, 3959–3972.

Lee, S., Park, J.-Y., Lee, W.-H.a, Kim, H.o, Park, H.-C., Mori, K., & Suk, K. (2009). Lipocalin-2 is an autocrine mediator of reactive astrocytosis. *Journal of Neuroscience*, **29**(1), 234–249.

Li, L., Lundkvist, A., Andersson, D., Wilhelmsson, U., Nagai, N., Pardo, A. C., Nodin, C., Ståhlberg, A., Aprico, K., Larsson, K., Yabe, T., Moons, L., Fotheringham, A., Davies, I., Carmeliet, P., Schwartz, J. P., Pekna, M., Kubista, M., Blomstrand, F., Maragakis, N., Nilsson, M., & Pekny, M. (2008). Protective role of reactive astrocytes in brain ischemia. *Journal of Cerebral Blood Flow and Metabolism*, **28**(3), 468–481.

Lier, J., Streit, W. J., & Bechmann, I. (2021). Beyond Activation: Characterizing microglial functional phenotypes. *Cells*, **10**(9), 2236.

Lin, T. N., He, Y. Y., Wu, G., Khan, M., & Hsu, C. Y. (1993). Effect of brain edema on infarct volume in a focal cerebral ischemia model in rats. *Stroke*, **24**(1), 117–121.

Liu, C.-W., Wang, E. Y., Wang, H.-L., Liao, K. H., Chen, H.-Y., Chen, H. S., & Lai, T. W. (2022). Blood-brain barrier disruption in preclinical mouse models of stroke can be an experimental artifact caused by craniectomy. *eNeuro*, **9**(5), ENEURO.0343–22.2022.

Manley, G. T., Fujimura, M., Ma, T., Noshita, N., Filiz, F., Bollen, A. W., Chan, P., & Verkman, A. S. (2000). Aquaporin-4 deletion in mice reduces brain edema after acute water intoxication and ischemic stroke. *Nature Medicine*, **6**(2), 159–163.

Mathiisen, T. M., Nagelhus, E. A., Jouleh, B., Torp, R., Frydenlund, D. S., Mylonakou, M.-N., Amiry-Moghaddam, M., Covolan, L., Utvik, J. K., Riber, B., Gujord, K. M., Knutsen, J., Ø, S., Laake, P., Davanger, S., Haug, F.-M., Rinvik, E., & Ottersen, O. P. (2006). Postembedding Immunogold Cytochemistry of Membrane Molecules and Amino Acid Transmitters in the Central Nervous System. In *Neuroanatomical Tract-Tracing 3: Molecules, Neurons, and Systems*, ed. Zaborszky L, Wouterlood FG & Lanciego JL, pp. 72–108. Springer US, Boston, MA.

Moskowitz, M. A., Lo, E. H., & Iadecola, C. (2010). The science of stroke: Mechanisms in search of treatments. *Neuron*, **67**(2), 181–198.
Nagelhus, E. A., & Ottersen, O. P. (2013). Physiological roles of aquaporin-4 in brain. *Physiological Reviews*, **93**(4), 1543–1562.
Nielsen, S., Arnulf Nagelhus, E., Amiry-Moghaddam, M., Bourque, C., Agre, P., & Ottersen, O. P. (1997). Specialized membrane domains for water transport in glial cells: high-resolution immunogold cytochemistry of aquaporin-4 in rat brain. *Journal of Neuroscience*, **17**(1), 171–180.
Papadopoulos, M. C., & Verkman, A. S. (2007). Aquaporin-4 and brain edema. *Pediatric Nephrology*, **22**(6), 778–784.
Papadopoulos, M. C., & Verkman, A. S. (2013). Aquaporin water channels in the nervous system. *Nature Reviews Neuroscience*, **14**(4), 265–277.
Prydz, A., Stahl, K., Zahl, S., Skauli, N., Skare, Ø., Ottersen, O. P., & Amiry-Moghaddam, M. (2020). Pro-inflammatory role of AQP4 in mice subjected to intrastriatal injections of the parkinsonogenic toxin MPP. *Cells*, **9**(11), 2418.
Rao, S. B., Katoozi, S., Skauli, N., Froehner, S. C., Ottersen, O. P., Adams, M. E., & Amiry-Moghaddam, M. (2019). Targeted deletion of beta1-syntrophin causes a loss of Kir 4.1 from Muller cell endfeet in mouse retina. *Glia*, **67**(6), 1138–1149.
Schmidt, U., Weigert, M., Broaddus, C. &., & Myers, G. (2018). Cell Detection with Star-Convex Polygons. In *Medical Image Computing and Computer Assisted Intervention – MICCAI 2018*, ed. Frangi AF, Schnabel JA, Davatzikos C, Alberola-López C & Fichtinger G, pp. 265–273. Springer International Publishing, Cham.
Schneider, C. A., Rasband, W. S., & Eliceiri, K. W. (2012). NIH Image to ImageJ: 25 years of image analysis. *Nature Methods*, **9**(7), 671–675.
Suk, K. (2016). Lipocalin-2 as a therapeutic target for brain injury: An astrocentric perspective. *Progress in Neurobiology*, **144**, 158–172.
Thrane, A. S., Rappold, P. M., Fujita, T., Torres, A., Bekar, L. K., Takano, T., Peng, W., Wang, F., Rangroo Thrane, V., Enger, R., Haj-Yasein, N. N., Skare, Ø., Holen, T., Klungland, A., Ottersen, O. P., Nedergaard, M., & Nagelhus, E. A. (2011). Critical role of aquaporin-4 (AQP4) in astrocytic Ca2+ signaling events elicited by cerebral edema. *Proceedings of the National Academy of Sciences, USA*, **108**(2), 846–851.
Williamson, M. R., Fuertes, C. J. A., Dunn, A. K., Drew, M. R., & Jones, T. A. (2021). Reactive astrocytes facilitate vascular repair and remodeling after stroke. *Cell reports*, **35**(4), 109048.
Xiong, X.-Y.i, Liu, L., & Yang, Q.-W.u (2016). Functions and mechanisms of microglia/macrophages in neuroinflammation and neurogenesis after stroke. *Progress in Neurobiology*, **142**, 23–44.
Yao, X., Derugin, N., Manley, G. T., & Verkman, A. S. (2015). Reduced brain edema and infarct volume in aquaporin-4 deficient mice after transient focal cerebral ischemia. *Neuroscience Letters*, **584**, 368–372.

Additional information

Data availability statement

The data that support the findings of this study are available from the corresponding author upon reasonable request.

Competing interests

Authors declare no competing interest.

Author contributions

Conceptualization: M.A.M. Data curation: N.S., N.Z., S.B. Formal Analysis: N.S., N.Z., S.B., M.S., M.A.M., O.P.O. Funding Acquisition: M.A.M. Investigation: N.S., N.Z., S.B., M.S. Methodology: N.S., N.Z., S.B., S.G., S.B.R., M.S. Project administration: M.A.M. Resources: M.A.M., C.M., O.P.O. Software: S.B., Supervision: M.A.M., C.M., S.B.R., O.P.O. Validation: N.S., S.B., M.A.M. Visualization: N.S., N.Z., S.B., M.S. Writing – original draft: M.A.M., N.S., N.Z., S.B., O.P.O. Writing – review and editing: N.S., N.Z., S.B., S.G., M.S., S.B.R., C.M., M.A.M., O.P.O. All authors approved the final version of the manuscript; agree to be accountable for all aspects of the work in ensuring that questions related to the accuracy or integrity of any part of the work are appropriately investigated and resolved; and all persons designated as authors qualify for authorship, and all those who qualify for authorship are listed.

Funding

This work was supported by Olav Thon Stiftelsen (Olav Thon Foundation): Mahmood Amiry-Moghaddam, 16-1606.

Acknowledgements

The authors would like to thank Mina Martine Frey, Gezime Seferi, Hanne Guldsten, Bashir Hakim, and Grazyna Babinska for technical assistance

Keywords

aquaporin-4, astrocyte, dMCAO, GFAP, LCN2, microglia, neuroinflammation

Supporting information

Additional supporting information can be found online in the Supporting Information section at the end of the HTML view of the article. Supporting information files available:

Peer Review History